

FULL PAPER

Open Access



Influence of geomagnetic storms on the quality of magnetotelluric impedance

Hao Chen^{1*} , Hideki Mizunaga² and Toshiaki Tanaka²

Abstract

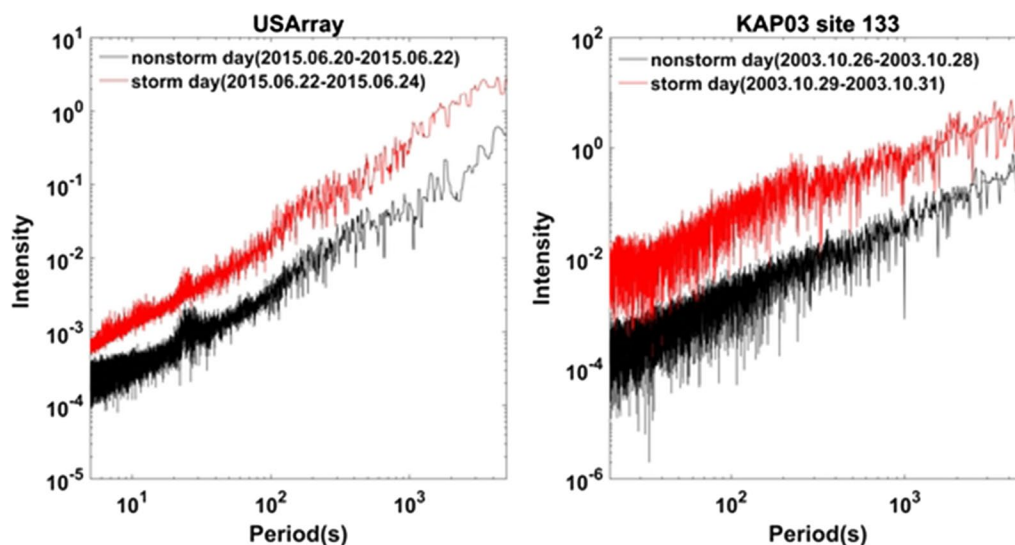
Magnetotelluric (MT) field data contain natural electromagnetic signals and artificial noise sources (instrumental, anthropogenic, etc.). Not all available time-series data contain usable information on the electrical conductivity distribution at depth with a low signal-to-noise ratio. If variations in the natural electromagnetic signal increase dramatically in a geomagnetic storm, the signal-to-noise ratio increases. A more reliable impedance may be obtained using storm data in a noisy environment. The field datasets observed at mid-latitudes were used to investigate the effect of geomagnetic storms on MT impedance quality. We combined the coherence between the electric and magnetic fields and the result of the MT sounding curve to evaluate the MT impedance quality across all periods and combined the phase difference among the electric and magnetic fields, the polarization direction, and the hat matrix to discuss the data quality for a specific period simultaneously. The case studies showed that the utilization of the data observed during the geomagnetic storm could overcome the local noise and bring a more reliable impedance.

Keywords: Geomagnetic storm, Impedance tensor, Magnetotelluric method

*Correspondence: chenhaomagnetic@gmail.com

¹ Department of Earth Resources Engineering, Graduate School of Engineering, Kyushu University, Fukuoka 819-0395, Japan
Full list of author information is available at the end of the article

Graphical Abstract



Introduction

The magnetotelluric (MT) method is a passive electromagnetic (EM) method used to infer the subsurface electrical conductivity from natural geomagnetic and geoelectric fields observed on Earth's surface. It was first proposed by Rikitake (1948), Cagniard (1953) and Tikhonov (1950). Many works have focused on the Earth's EM environment, e.g., Constable (2016), Constable and Constable (2004), Garcia and Jones (2002), Hennessy and Macnae (2018), Mareschal (1986), and McPherron (2005). Generally, high-frequency signals (> 1 Hz) originate from worldwide thunderstorm activity. In comparison, the low-frequency signals (< 1 Hz) originate from the interaction between solar winds and the Earth's magnetosphere and ionosphere. The MT method assumes that the EM source is located at a large distance from the observation area, and the signal propagates as plane waves. This condition is also known as the far-field assumption (Oettinger et al. 2001; Zonge and Hughes 1987) and is dependent on the target period. The natural EM signal from the magnetosphere and ionosphere or global lighting is far from the observation site and can be treated as plane waves. In contrast, the local anthropogenic sources violate the plane wave assumption and are regarded as noise in the MT method. Szarka (1988) and Junge (1996) summarized the active and passive noise sources observed in MT measurements.

Not all MT time-series data include usable information on the electrical conductivity distribution at depth. A low signal-to-noise ratio (SNR) can occur when the natural signal level is comparable to or below the instrument noise level or in the presence of some types of cultural noise (Chave and Jones 2012). The first step in MT data processing is estimating the frequency-domain impedance tensor from the measured time-series data. All MT data interpretations are based on the impedance. Therefore, it is very important to obtain a reliable impedance. When the noise continuously contaminates the site, it is not easy to obtain a reliable impedance from the current MT data processing technology (Chave et al. 1987; Chave and Thomson 2003, 2004; Egbert 1997; Egbert and Booker 1986; Smirnov 2003; Weckmann et al. 2005).

A geomagnetic storm is a temporary disturbance of Earth's geomagnetic field caused by the interactions between the solar wind and the magnetosphere–ionosphere system. It starts when the enhanced energy of the solar wind is transferred into the magnetosphere (Chave and Jones 2012; Tsurutani et al. 2006). The disturbance storm time (*Dst*) is an index of magnetic activity derived from the four low-latitude horizontal magnetic fields (Sugiura and Kamei 1991). The *Dst* can indicate the occurrences of magnetic storms and their severity. When the *Dst* is below -50 nT, it is categorized as a geomagnetic storm. When the *Dst* is below -100 nT, it is categorized as a strong geomagnetic storm (Singh et al. 2017). During

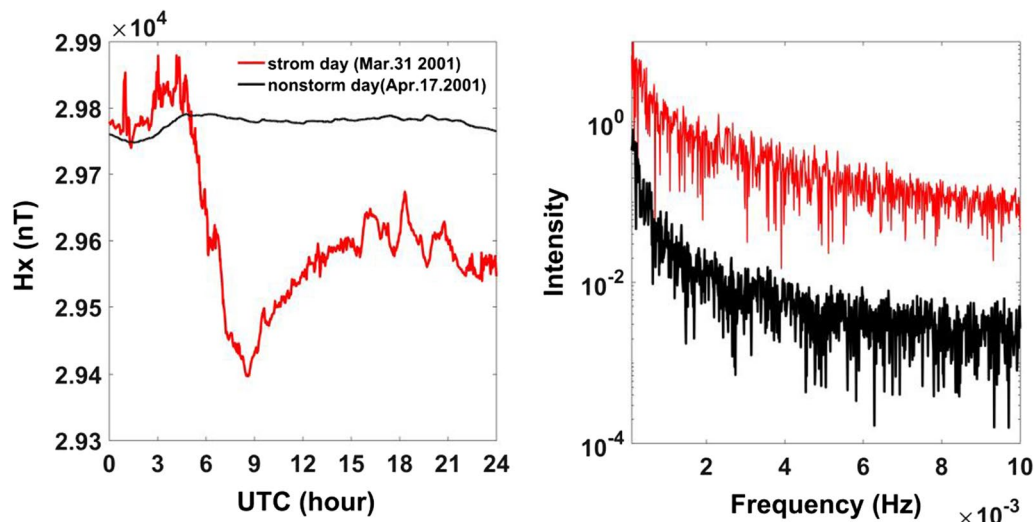


Fig. 1 Geomagnetic intensities along the N–S direction during the storm and non-storm days. The black lines denote the non-storm day data, and the red lines denote the storm day data. The left panel shows a profile in the time domain, and the right panel shows the spectrum in the frequency domain

a strong geomagnetic storm, the variation in the natural EM signal increases substantially. Figure 1 shows the geomagnetic intensities along the N–S direction during storm and non-storm days at Japan's Kakioka (KAK) station. The geomagnetic field is depressed during the storm and gradually recovers to its average level. Its intensity observed during the storm day is almost two orders of magnitude stronger than that during the non-storm day. Noise can be neglected under this condition. High SNR data can be obtained even with artificial noise, depending on the strength of the geomagnetic storm and the noise.

It is well known in MT communities that the natural EM signal increases significantly during a strong geomagnetic storm. However, examples of evaluating the effects of geomagnetic storms on the MT impedance quality are rare. The plane wave assumption is generally acceptable at mid-latitudes during geomagnetic storms (Lezaeta et al. 2007; Viljanen et al. 1993). However, it is violated at high magnetic latitudes because the source field is nonuniform during geomagnetic storms (Mareschal 1981; Viljanen et al. 1993; Garcia et al. 1997; Lezaeta et al. 2007). There is another issue that the geomagnetic pulsations (Pcs) in the Pc3–4 band (~ 10 – 100 s) at mid-latitudes associated with field-line resonances can violate the fundamental assumption of the MT method over resistive regions, where the skin depths are large (Egbert et al. 2000; Murphy and Egbert 2018). However, this issue is not the focus of this paper. Possible biases in the MT transfer function due to the source effect are considered only at long periods ($> 1,000$ s) and near the

auroral or equatorial electrojets (Murphy and Egbert 2018). We focus on investigating the effects of geomagnetic storms on the MT impedance between 1 and 1000 s at the midlatitude.

Our hypothesis of the geomagnetic storm is beneficial to MT impedance quality at mid-latitudes. In a quiet EM environment, no matter whether there is a geomagnetic storm, we can get a reliable MT impedance tensor. On the other hand, in a noisy EM environment, we may fail to get a reliable impedance tensor during a non-storm day, while the SNR becomes high during a storm day, and a reliable impedance result may be obtained by using the storm data. This paper investigates this hypothesis by comparing the data quality at a specific frequency and MT impedance quality during the storm and non-storm days using field datasets observed at mid-latitudes.

Parameters to evaluate the data quality

Coherence is an important parameter often used for analyzing data quality (e.g., Egbert and Livelybrooks 1996; Fontes et al. 1988; Jones and Jödicke 1984). In general, we can combine the performance of impedance and coherence to estimate the MT impedance quality across all periods; we also combine the phase difference between the electric and magnetic fields, the polarization direction, and the hat matrix to discuss the data quality for a specific period simultaneously.

Impedance tensor

In the MT method, the magnetic field (H) and the electric field (E) have a linear relationship in the frequency

domain. The impedance tensor \mathbf{Z} relates the electric and magnetic fields as follows:

$$\begin{pmatrix} E_x(\omega) \\ E_y(\omega) \end{pmatrix} = \begin{pmatrix} Z_{xx}(\omega) & Z_{xy}(\omega) \\ Z_{yx}(\omega) & Z_{yy}(\omega) \end{pmatrix} \begin{pmatrix} H_x(\omega) \\ H_y(\omega) \end{pmatrix} = \mathbf{Z}\mathbf{H}, \quad (1)$$

where \mathbf{E} and \mathbf{H} are the horizontal electric and magnetic fields at a specific frequency, respectively. ω denotes the angular frequency, x denotes the north–south direction, and y denotes the east–west direction.

The bounded influence remote reference processing code (BIRRP; Chave et al. 1987; Chave and Thomson 2003, 2004) is a typical conventional robust estimator to calculate the impedance tensor based on windowed FFT. We used the BIRRP code to calculate the impedance in this research and adopted the standard M-estimator (Chave et al. 1987).

The MT sounding curves are the most important result for discussing MT impedance quality. We expect MT sounding curves to be smooth as a function of frequency from the underlying physics because EM propagation in the conductive Earth is a diffusive process.

Phase difference and coherence between the electric and magnetic fields

The MT time-series data are observed simultaneously in several channels. Each channel is divided into N segments, and we can obtain N spectra by applying the Fourier transform to each segment. In polar coordinates, the cross-power spectra between two spectra A_i and B_i are expressed as follows:

$$A_i \bar{B}_i = |A_i| \cdot |B_i| e^{j(\varphi_{A_i} - \varphi_{B_i})}, \quad (2)$$

where j denotes the imaginary number unit, i ($=1, 2, \dots, N$) is the number index; A_i and B_i are the spectra calculated from the i^{th} segment from the different channels; and φ_{A_i} and φ_{B_i} denote the phases of A_i and B_i , respectively. The overline denotes the complex conjugate. On the other hand, the autopower spectra are expressed as follows:

$$A_i \bar{A}_i = |A_i|^2, B_i \bar{B}_i = |B_i|^2. \quad (3)$$

The phase difference between A_i and B_i ($PD(A_i, B_i)$) is calculated as follows:

$$\theta_i = \varphi_{A_i} - \varphi_{B_i} = \arg\left(e^{j(\varphi_{A_i} - \varphi_{B_i})}\right) = \arg\left(\frac{A_i \bar{B}_i}{|A_i| |B_i|}\right), \quad (4)$$

where θ_i denotes the angle of the phase difference (PD) between the two spectra at a specific frequency.

Coherence is the ratio between the cross-power spectral density and the root of the autopower spectral density. For the \mathbf{A} and \mathbf{B} spectrum at a specific frequency, it is defined as follows:

$$\text{Coh}(\mathbf{A}, \mathbf{B}) = \frac{|\langle \mathbf{A} \bar{\mathbf{B}} \rangle|}{\sqrt{\langle \mathbf{A} \bar{\mathbf{A}} \rangle \langle \mathbf{B} \bar{\mathbf{B}} \rangle}}, \quad (5)$$

where the brackets represent the averages of N individual autopower spectra and cross-power spectra. For instance,

$$\langle \mathbf{A} \bar{\mathbf{B}} \rangle = \frac{1}{N} \sum_{i=1}^N A_i \bar{B}_i. \quad (6)$$

Coherence is a quantitative measure of the phase difference (PD) consistency between the two channels. If two channels are coherent, their phases must be the same or have a constant difference (Marple and Marino 2004). That means there is a preferred direction of the phase difference when two channels are coherent.

In a certain geological situation, the impedance tensor is shown in Table 1. The diagonal element of impedance is zero in the 1-D or 2-D models (when the observation axes coincide with the geoelectrical strike). The relationship between the orthogonal electric and magnetic fields for the north–south direction is as follows:

$$E_{x_i} = Z_{xy} H_{y_i}. \quad (7)$$

That means in the case of the 1-D or 2-D structure in a quiet environment (1-D/2-D case), the orthogonal electric and magnetic fields are coherent and have a constant PD, and the PD equals the impedance phase.

Table 1 Impedance tensor characteristics in certain geological situations. In the 1-D case, the impedance of the diagonal elements is zero. In the 2-D case, when the observation axes coincide with the geoelectrical strike, the impedance is zero in the diagonal elements, and the off-diagonal elements are unequal. In the 3-D case, all \mathbf{Z} values are nonzero

1-D structure	2-D structure	3-D structure
$\begin{pmatrix} 0 & Z_{xy} \\ Z_{yx} & 0 \end{pmatrix}$	$\begin{pmatrix} 0 & Z_{xy} \\ Z_{yx} & 0 \end{pmatrix}$	$\begin{pmatrix} Z_{xx} & Z_{xy} \\ Z_{yx} & Z_{yy} \end{pmatrix}$
$Z_{xy} = -Z_{yx}$	$Z_{xy} \neq Z_{yx}$	All \mathbf{Z} values are nonzero

In the 2-D (when the observation axes do not coincide with the geoelectrical strike) or 3-D cases, all impedance values are nonzero, and for the north–south direction, there is a relationship between the electric and magnetic fields as follows:

$$E_{x_i} = Z_{xx}H_{x_i} + Z_{xy}H_{y_i}. \quad (8)$$

There is no direct relationship between E_x and H_x and between E_y and H_y , which is very complex in real field data.

On the other hand, the case of phase rolling out of the quadrant (PROQ) (Chouteau and Tournier 2000; Weckmann et al. 2003; Yu et al. 2019) is increasingly recognized in MT field surveys. The channeling current caused by complex 3-D isotropic media can explain the PROQ phenomenon. The characteristic of PROQ is that the parallel electric and magnetic fields are coherent, while the orthogonal components are incoherent.

Although PD and coherence are different in different situations, they are useful parameters for discussing data quality.

Polarization directions

Weckmann et al. (2005) showed the effectiveness of using the polarization directions to estimate the background noise. The polarization directions for the magnetic field (α_H) at a specific frequency (Fowler et al. 1967) are defined as follows:

$$\alpha_{H_i} = \tan^{-1} \frac{2\text{Re}(H_{x_i}\overline{H_{y_i}})}{|H_{x_i}|^2 - |H_{y_i}|^2} = \tan^{-1} \frac{2\frac{|H_{x_i}|}{|H_{y_i}|} \cdot \cos(\theta_i)}{1 - \left(\frac{|H_{y_i}|}{|H_{x_i}|}\right)^2}, \quad (9)$$

where H_{x_i} and H_{y_i} are the spectra calculated from the i -th segment in the magnetic field and θ_i denotes the PD between H_{x_i} and H_{y_i} . The polarization direction is related to the phase difference and amplitude ratio between the two orthogonal fields.

A variety of sources generate natural magnetic signals. These sources generate magnetic fields that vary in their incident directions and amplitude. The phase difference and amplitude ratio between the two orthogonal magnetic fields vary with time; thus, the magnetic field has no preferred polarization direction (Weckmann et al. 2005).

In contrast, the local EM noise source usually has a constant location; the incident direction and energy have similar properties changing with time. Suppose that there is a preferred polarization direction for the magnetic field; we can consider that the coherent noise contaminates the data. On the other hand, when the incoherent noise contaminates the field data, the magnetic field has no preferred polarization direction. Therefore, the

polarization direction for the magnetic field can only detect coherent noise.

Hat matrix

The hat matrix is an N by N matrix (N denotes the sample of data) defined as follows (Chave and Thomson 2003, 2004):

$$H_{\text{hat}} = H(H^\dagger H)^{-1}H^\dagger, \quad (10)$$

where H represents N by two matrices of the horizontal magnetic field (H_x, H_y) at a specific frequency. The superscript \dagger denotes the complex conjugate transpose. The expected value of the hat matrix's diagonal element is $2/N$. The hat matrix is widely used to detect abnormal large-value data. We adopted the hat matrix to examine the energy variation of each segment (see the example in Fig. 4), and the data whose hat matrix's diagonal element was over the expected value ($2/N$) were defined as the leverage point in this research.

Case studies in two MT fields

In the case studies, we choose an intensive geomagnetic storm in the first case study and a less intensive one in the second case study. At last, the difference in the effect of the geomagnetic storm on the impedance quality is discussed in the discussion section.

Case study 1: KAP03, South Africa

The first field dataset used the 5-component MT time-series data observed at Kaapvaal in 2003 (KAP03). The 26 sites are distributed in a NE–SW profile, as shown in Fig. 2. The sampling period of this survey is 5 s. The data

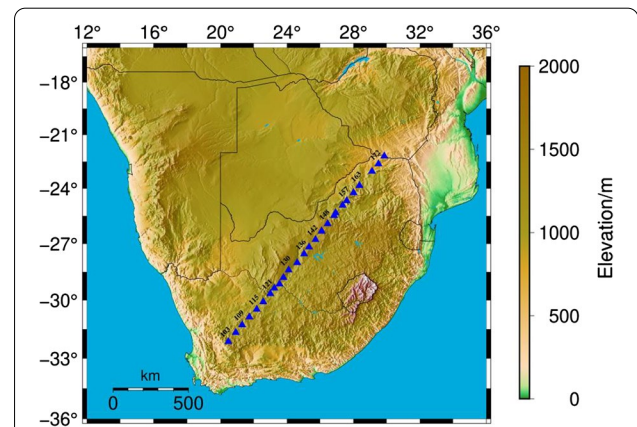
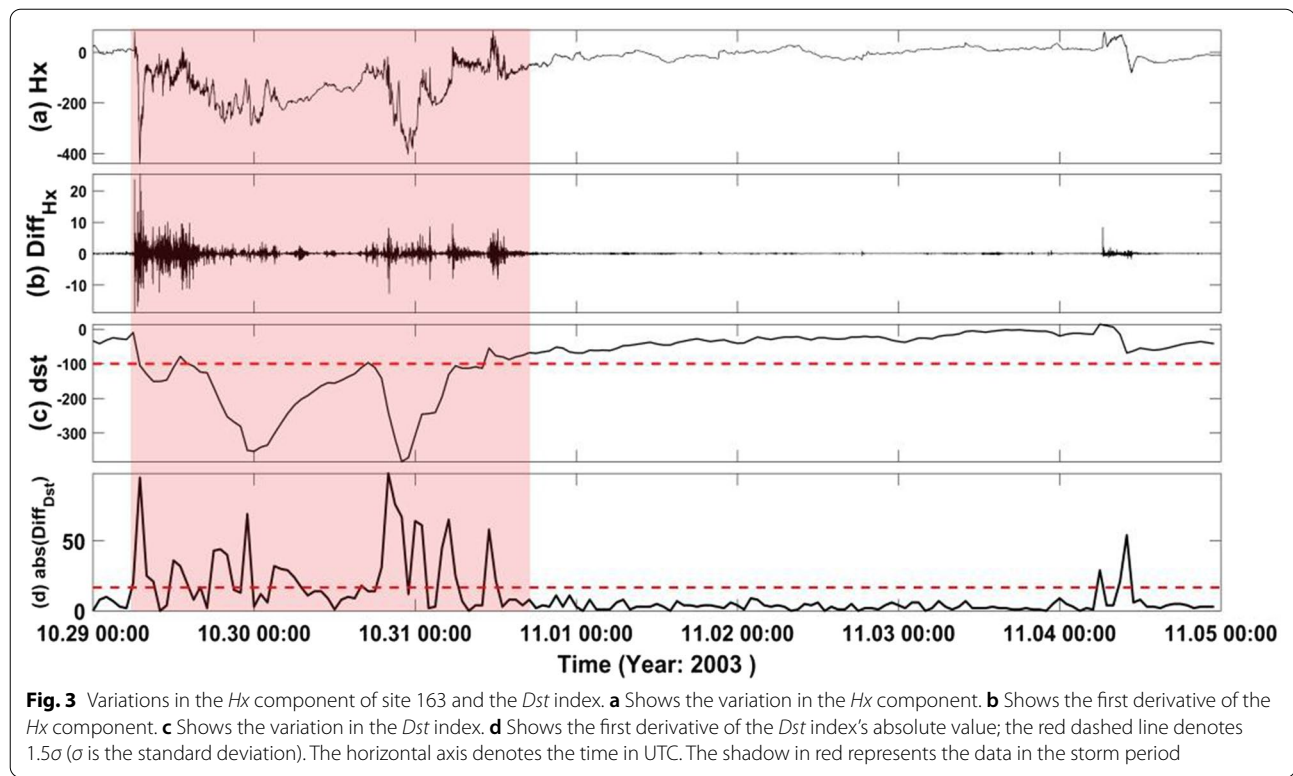


Fig. 2 Location map of KAP03. The blue triangles denote the observation site. Data for the sites in the middle of the profile (site 127–site 145 of KAP03) were heavily contaminated by direct current (DC) signals



were recorded for almost a month at each site as a part of the SAMTEX project (Jones et al. 2009). Data for the sites in the middle of the profile (site 127–site 145 of KAP03) were heavily contaminated by direct current (DC) signals from the DC train line running between Kimberley and Johannesburg (MTNET, see the website in references). During the observation period, a geomagnetic storm occurred around October 29 to October 31.

At first, we investigate the relationship of the variation between the time-series data and the Dst index. The following first difference filter is used to remove the trends and means of the signal x :

$$Diff(x_i) = x_i - x_{i-1}, \quad (11)$$

where i denotes the number of the time-series data. The absolute value of $Diff(x)$ can represent the strength of the fluctuation. In addition, the threshold k ($k = 1.5\sigma$) is used to detect abnormally high values, where σ is the standard deviation. A common approach is to take $\sigma = MAD/0.44845$, where MAD is the median of the absolute deviations from the data's median and $MAD = median(|x_i - median(x)|)$ (Chave and Thomson 2003). Figure 3 shows the time variations in the H_x component at site 163 and the Dst index. The red dashed line in Fig. 3d denotes the k used to detect the abnormally high value. The high absolute value of $Diff(Dst)$ corresponds to the high variation of $Diff(H_x)$ and the

storm. Therefore, we could use $Diff(Dst)$'s absolute value to detect the high variation data in the presence of a storm. This geomagnetic storm started at approximately 06:00 on October 29 and ended at approximately noon on October 31. We extracted 2-day data from 06:00 on October 29 to 06:00 on October 31 as the storm data.

Moreover, we investigate the relationship between the magnetic field amplitude and the hat matrix's diagonal elements at a specific frequency. The time-series data are divided into segments. We can obtain one spectrum by applying the Fourier transform to one segment. When performing the Fourier transform, there is the following relationship:

$$f = n * fs / L, \quad (12)$$

where f is the frequency corresponding to the n -th complex coefficient, n is the n -th complex coefficient in the spectrum, fs denotes the sampling rate, and L denotes the segment length. Each data in the frequency domain is calculated by each segment at a different time; the data in the frequency domain corresponds to the time; therefore, we plot the data by the time in the following data quality analysis at a specific frequency. Figure 4 compares the variations in the magnetic field amplitude and the hat matrix's diagonal elements in the period of 101 s using the data observed at site 163 from 00:00 on October 29 to 00:00 on November 4. It shows that the

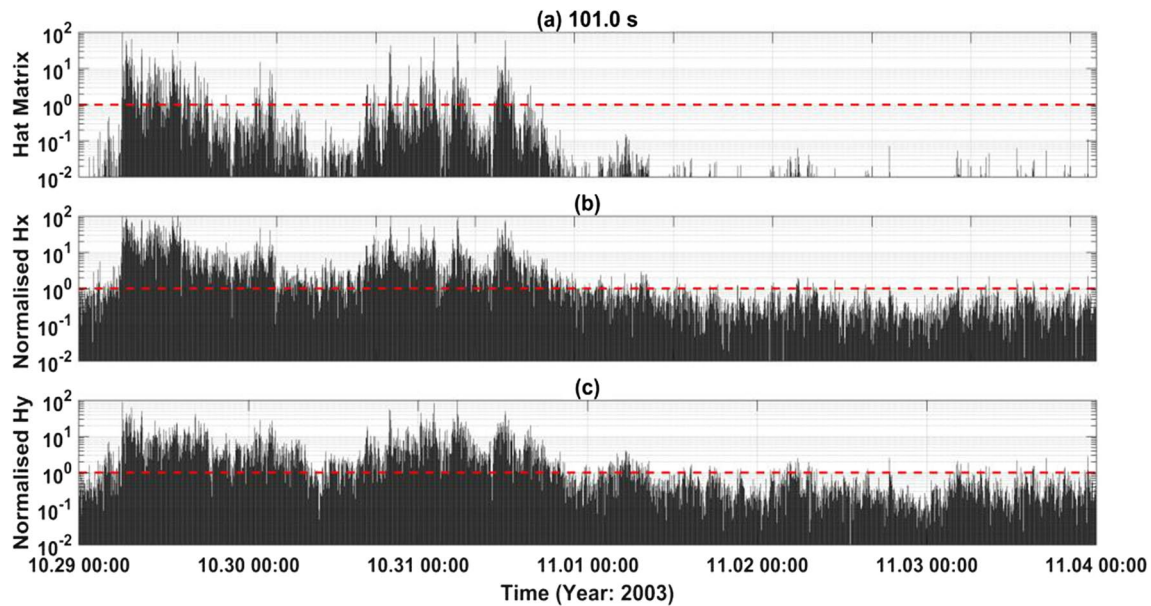


Fig. 4 Variations in the magnetic field amplitude and the hat matrix's diagonal elements in the period of 101 s using the data observed at site 163 from 00:00 on October 29 to 00:00 on November 4. **a** Shows the hat matrix's diagonal elements normalized by the expected value $2/N$. **b, c** Show the magnetic fields normalized by the standard deviation in the x- and y-directions, respectively. The variation in the hat matrix's diagonal elements has the same trend as the magnetic field amplitude

energy of the magnetic field is much stronger than that during the non-storm days. On the other hand, the variation of the hat matrix's diagonal elements has the same trend as the magnetic field amplitude. Therefore, we use the hat matrix to show the energy variation in the magnetic field and combine the phase difference between the electric and magnetic fields and polarization direction to discuss how the data quality varies with the energy in a specific period. In this research, the leverage point whose hat matrix's diagonal element exceeds the expected value ($2/N$) corresponds to a geomagnetic storm, and the corresponding data are shown in red in the following data quality analysis.

In the following case study, we use the data, including the geomagnetic storm, to investigate how the data quality varies with time in a specific frequency band first and then investigate the result of the impedance tensor calculated by the single-site processing and the remote-site processing at each site. On the one hand, we combine the phase difference between the electric and magnetic fields, the polarization direction, and the hat matrix to discuss the data quality in a specific frequency band. On the other hand, we compare the MT sounding curves and coherence distributions during the storm and non-storm days to discuss the effect of the geomagnetic storm on the quality of the impedance tensor. Moreover, as remote-site processing result is usually more reliable, we also compare the MT sounding curves calculated by the

single-site processing and remote-site processing simultaneously. We first investigate the effect of the storm on the data quality and MT impedance quality in a quiet EM environment at site 163 and then investigate the effect in the noisy EM environment at sites 142 and 130.

Next, the data quality analysis at site 163 in the period of 101 s is shown in Fig. 5. The data observed from 00:00 on October 29 to 00:00 on November 4 is used. Panels (b) and (c) show that the PD between the orthogonal electric and magnetic fields ($PD(E_x, H_y)$, $PD(E_y, H_x)$) has a preferred direction, while the PD between the parallel electric and magnetic fields ($PD(E_x, H_x)$, $PD(E_y, H_y)$) is scattered all the time. The PD is more concentrated during the storm day than the non-storm day, and it coincides with the increase in the coherence value during the storm in Fig. 6j, k.

Next, we combine the impedance result and coherence distribution to discuss the MT impedance quality at site 163. Figure 6 shows the MT sounding curves and coherence distributions during the storm and non-storm days. The data observed from 00:00 on November 1 to 00:00 on November 4 are used as the non-storm data. The coherence values between the orthogonal electric and magnetic fields ($Coh(E_x, H_y)$ and $Coh(E_y, H_x)$) are high, while those between the parallel components ($Coh(E_x, H_x)$ and $Coh(E_y, H_y)$) are low across all periods. The data can be categorized into a 1-D/2-D case in a quiet environment during the storm and non-storm days. Because the

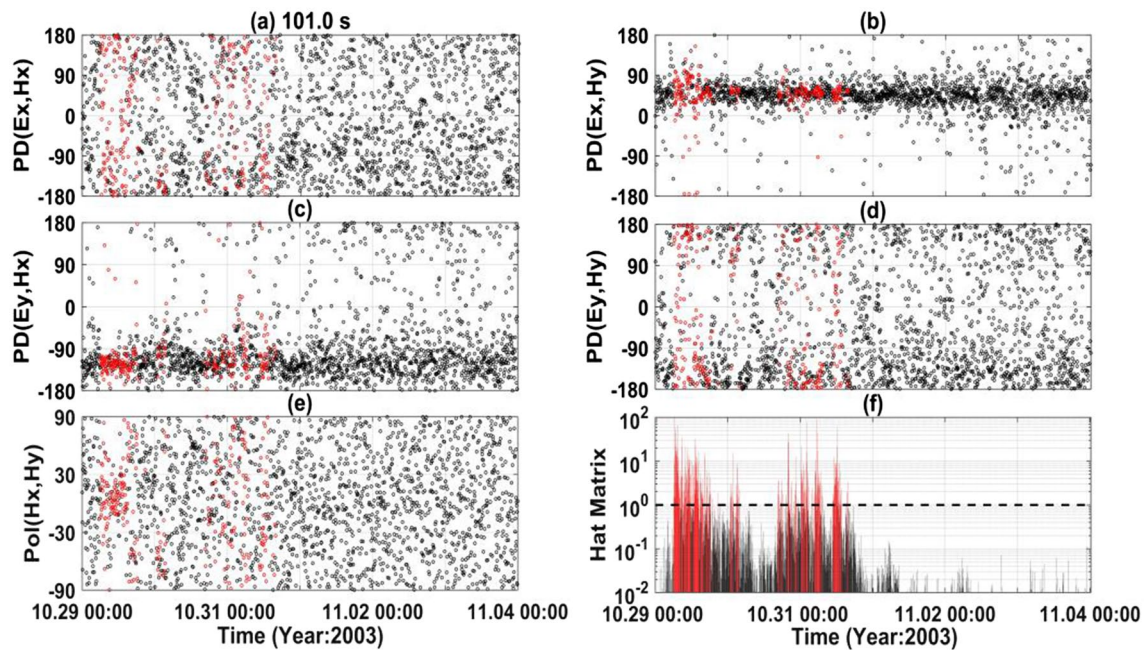


Fig. 5 Evaluation indices in the period of 101 s using the data observed at site 163 from 00:00 on October 29 to 00:00 on November 4. **a–d** Show the variation in $PD(E_x, H_x)$, $PD(E_x, H_y)$, $PD(E_y, H_x)$, and $PD(E_y, H_y)$; **e** shows the variation in polarization direction for the magnetic field; and panel (f) shows the variation in the normalized hat matrix's diagonal element. The data in red correspond to the leverage point, whose hat matrix diagonal element exceeds the expected value ($2/N$)

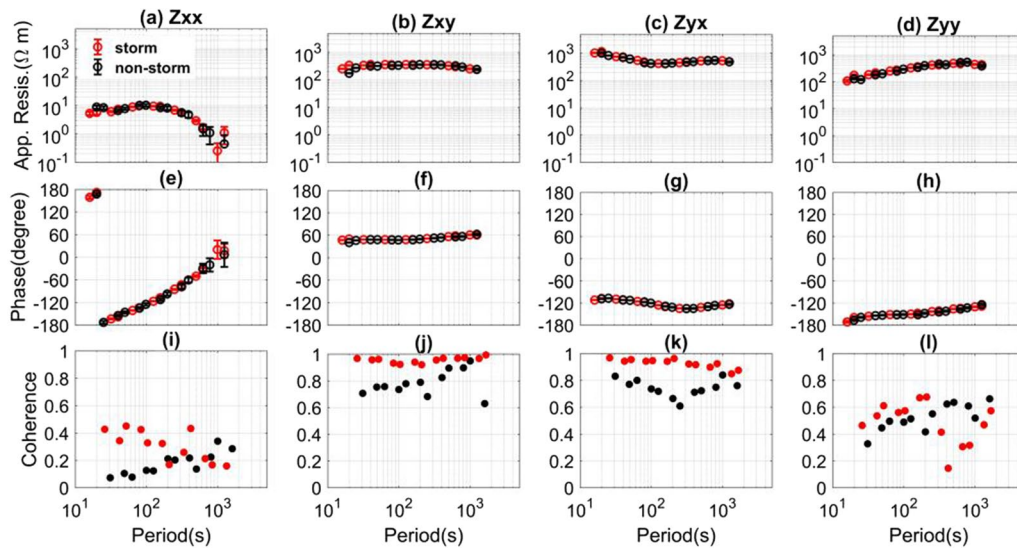


Fig. 6 MT sounding curves and coherence distributions during the storm and non-storm days using the data observed at site 163. The black color indicates the results calculated by the non-storm data observed from 00:00 on November 1 to 00:00 on November 4; the red color indicates the results calculated by storm data observed from 06:00 on October 29 to 06:00 on October 31. **a–d** Show the apparent resistivity. **e–h** Show the impedance phase. **i–l** Show the distribution of coherence. The horizontal axis denotes the period in seconds

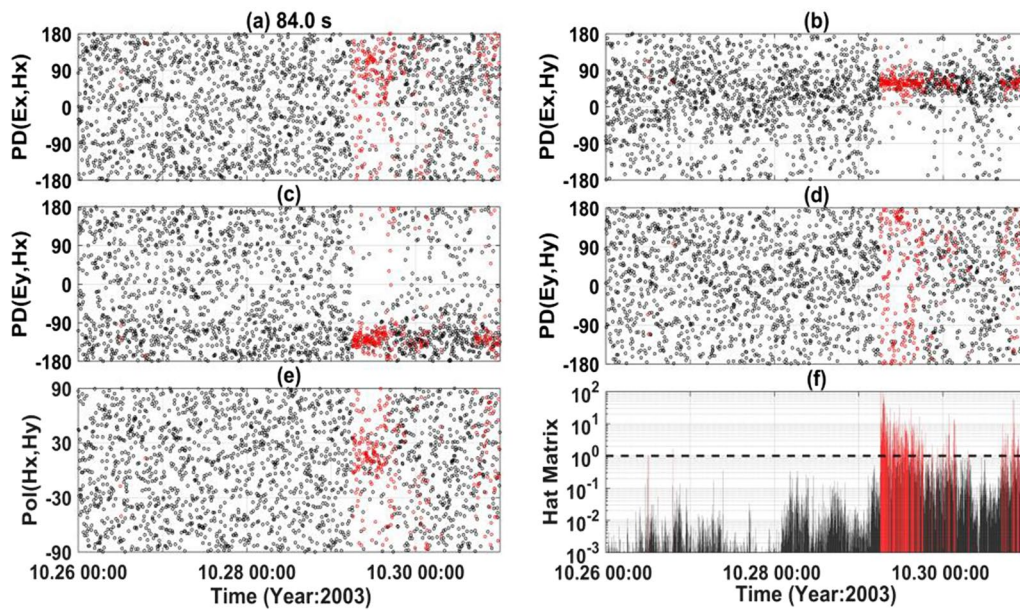


Fig. 7 Evaluation indices in the period of 84 s using the data observed from 00:00 on October 26 to 00:00 on October 31 at site 142. The data in red correspond to the leverage data caused by the storm. **a–d** Show the variation in $PD(E_x, H_x)$, $PD(E_x, H_y)$, $PD(E_y, H_x)$, and $PD(E_y, H_y)$, respectively; **e** shows the variation in polarization direction for the magnetic field; and **f** shows the variation in the normalized hat matrix's diagonal element. There are preferred directions of the phase difference between the orthogonal electric and magnetic fields corresponding to the leverage data, as shown in **b** and **c**

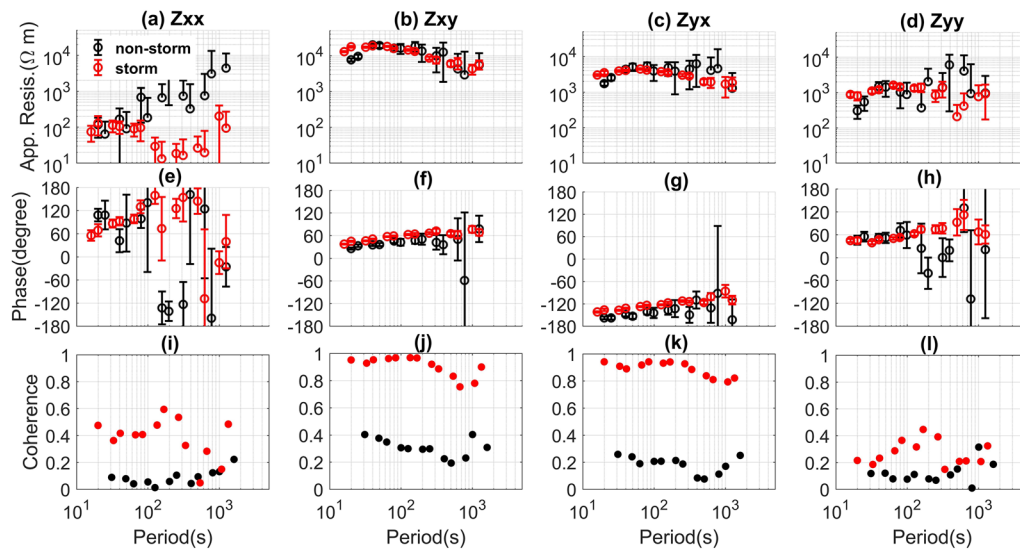


Fig. 8 MT sounding curves and coherence distributions during the storm and non-storm days using the data observed at site 142. The black color indicates the results calculated by the non-storm data observed from 00:00 on October 26 to 00:00 on October 29; the red color indicates the results calculated by storm data observed from 06:00 on October 29 to 06:00 on October 31

environment is quiet, the proportion of high SNR data is high enough to obtain a reliable impedance during the storm and non-storm days; therefore, the MT impedance results calculated by storm and non-storm data coincide. We also compared the result with the remote reference results and found that both are similar. This example shows that the storm does not influence the impedance quality in a quiet EM environment.

And then, a similar analysis is performed at site 142. The data quality analysis in the period of 84 s is shown in Fig. 7. The data observed from 00:00 on October 26 to 00:00 on October 31 are used. The natural EM signal also varies significantly during the storm, as shown in panel (f). The SNR depends on the strength of the natural EM signal and noise. Therefore, the data during the storm may also contain data dominated by noise. Panels (b) and (c) show that the PD between the orthogonal electric and magnetic fields ($PD(E_x, H_y)$, $PD(E_y, H_x)$) has a preferred direction corresponding to the leverage point during the storm day. The data in red can be categorized into a 1-D/2-D case with a high SNR. The SNR of the black data is low, and all the PD is scattered. Incoherent noise may contaminate the data during the non-storm day.

Next, we discuss the MT impedance quality during the storm and non-storm days at site 142. Figure 8 shows the MT sounding curves and coherence distributions. The data observed from 00:00 on October 26 to 00:00 on October 29 are used as the non-storm data. The coherence is low during non-storm days, and it coincides with

the PD being scattered during non-storm days, as shown in Fig. 7a–d. It increased considerably and was close to one across all periods during the storm in the XY and YX components. The low coherence during the non-storm days could be attributed to incoherent noise. The storm MT sounding curve is smoother than the non-storm result in the XY and YX components, and the error bar is small. Both the XX and YY component is unstable. This storm result can be interpreted as a 1-D/2-D case with a high SNR.

Moreover, we compare the MT sounding curves calculated by single-site and remote reference data processing in Fig. 9. Site 151 is used as the remote reference site. The results calculated by storm data with and without remote reference processing coincide, while the non-storm-RR result, calculated by remote reference processing using the non-storm data, is scattered, and the error bar is also large. The impedance is biased using the non-storm data despite using remote reference data due to the continuous incoherent noise, according to the data quality analysis in Fig. 7. The data quality is improved during the storm, and we can obtain a reliable impedance even using single-site data processing.

Next, we do a similar analysis at site 130. The data quality analysis in the period of 84 s is shown in Fig. 10. The data observed from 00:00 on October 26 to 00:00 on October 31 is used. Panels (a), (b), (c) and (d) show a preferred direction of PD close to 0° or 180° , and there is a preferred direction of polarization at approximately

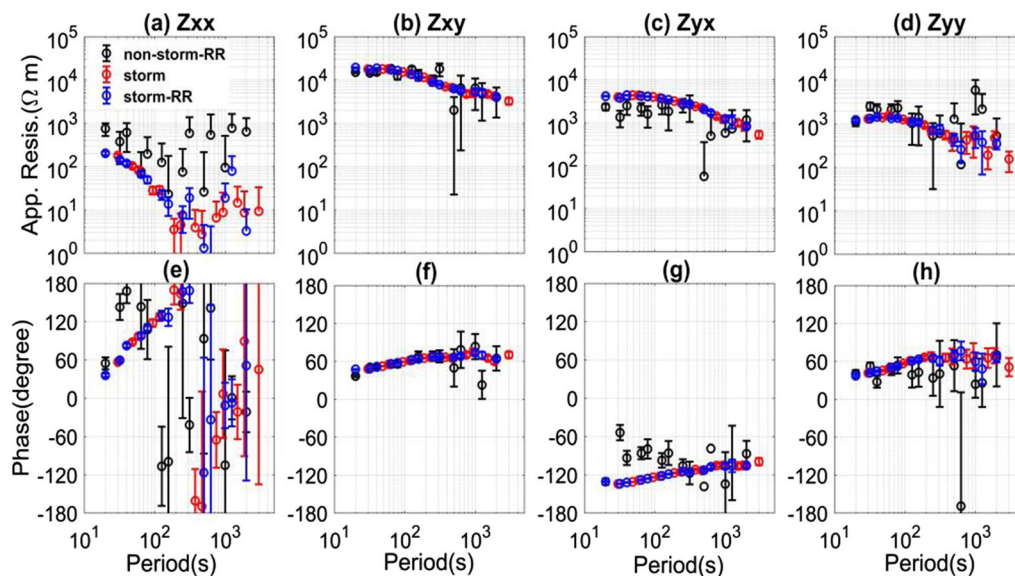


Fig. 9 Comparison of the MT sounding curves calculated by single-site and remote reference data processing using the storm and non-storm data observed at site 142. The black curves are calculated by the non-storm data with remote reference processing (non-storm-RR); the blue curves are calculated by storm data with remote reference processing (storm-RR); and the red curves are calculated by storm data with single-site data processing (storm). **a–d** Show the apparent resistivity. **e–h** Show the impedance phase. The horizontal axis denotes the period in seconds

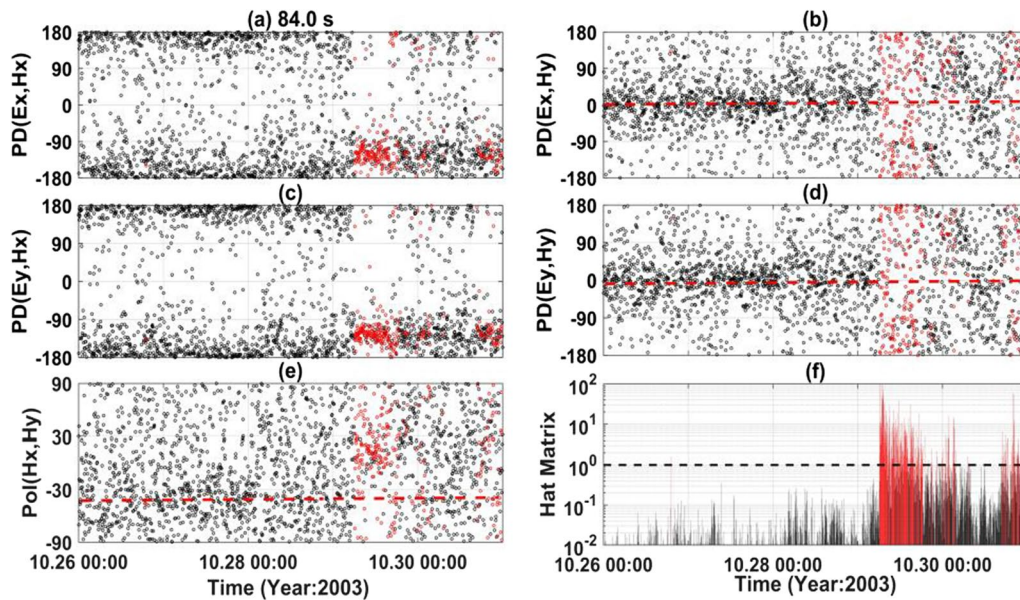


Fig. 10 Evaluation indices in the period of 84 s using the data observed at site 130 from 00:00 on October 26 to 00:00 on October 31. The data in red correspond to the leverage data associated with the storm. There are preferred directions of the phase difference between the electric and magnetic fields corresponding to the leverage data, as shown in **a** and **c**

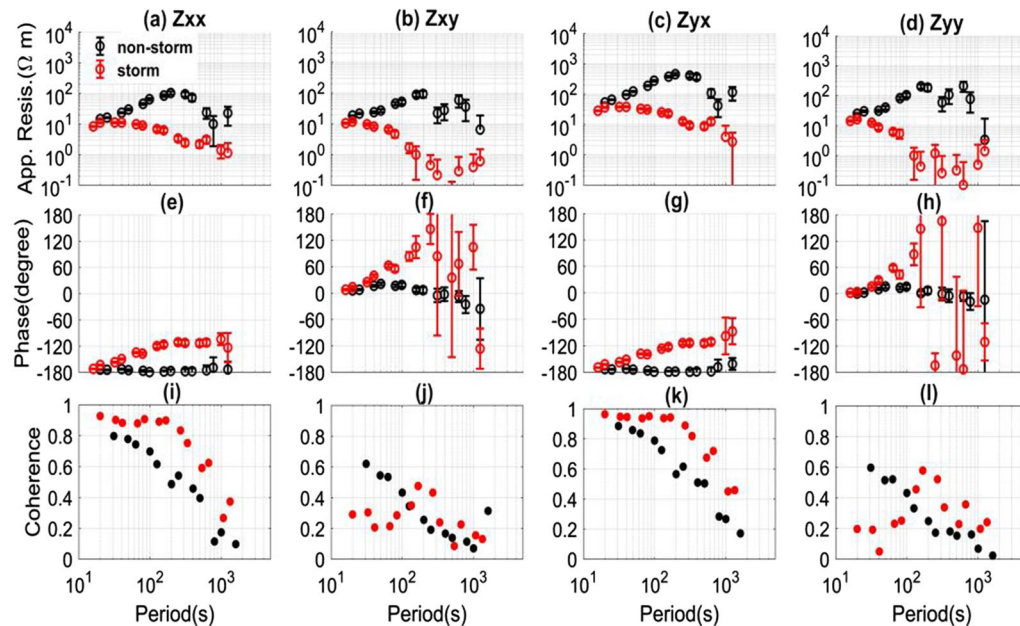


Fig. 11 MT sounding curves and coherence distributions during the storm and non-storm days using the data observed at site 130. The black color indicates the results calculated by the non-storm data observed from 00:00 on October 26 to 00:00 on October 29; the red color indicates the results calculated by storm data observed from 06:00 on October 29 to 06:00 on October 31

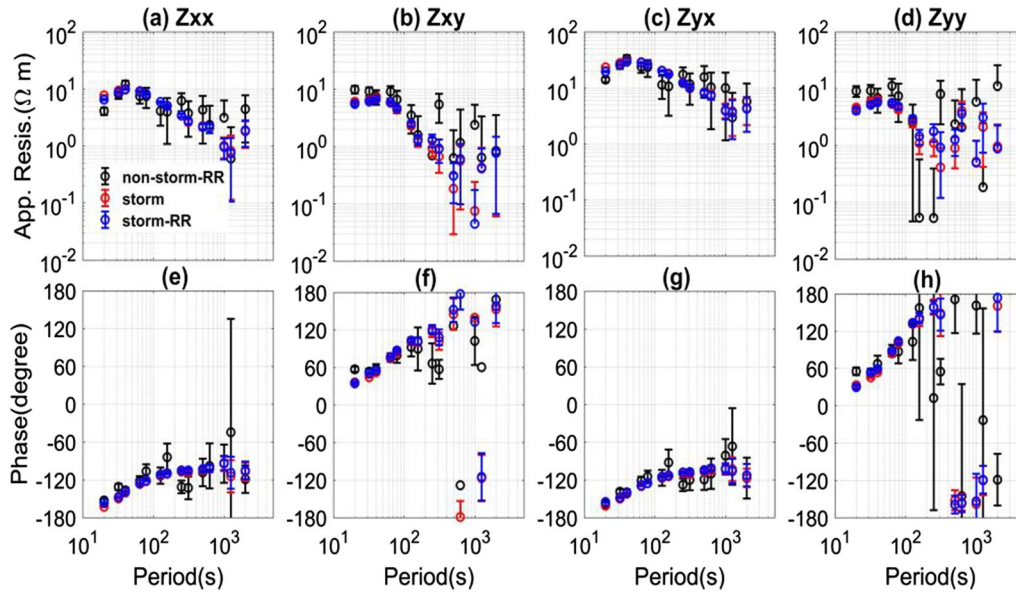


Fig. 12 Comparison of the MT sounding curves calculated by single-site and remote reference data processing using the storm and non-storm data observed at site 130. **a–d** Show the apparent resistivity. **e–h** Show the impedance phase. The horizontal axis denotes the period in seconds. The storm result and storm-RR result coincide and cover each other

– 30° during the non-storm day. The polarization direction variation indicates that the non-storm data are dominated by coherent noise during the non-storm day. On the other hand, the PD between the electric and magnetic fields ($PD(E_x, H_x)$ and $PD(E_y, H_x)$) has a preferred direction corresponding to the leverage point during the storm day. The enhanced natural EM signal may cause it.

Next, we discuss the MT impedance quality during the storm and non-storm days at site 130. Figure 11 shows the MT sounding curve and coherence distributions. The data observed from 00:00 on October 26 to 00:00 on October 29 are used as the non-storm data. The coherence values in $Coh(E_x, H_x)$ and $Coh(E_y, H_x)$ are high between 10 and 200 s during non-storm days; however, the XX and YX phases calculated by non-storm data are close to – 180°, and the apparent resistivity increases as a line on the log scale between 10 and 200 s, which represents a phenomenon of local noise (Zonge and Hughes, 1987). A value of – 180° would correspond to the grounded dipole noise sources (e.g., DC trains). On the other hand, the coherence value between the parallel electric and magnetic field $Coh(E_x, H_x)$ is high, while the coherence value between the orthogonal electric and magnetic field $Coh(E_x, H_y)$ is relatively low during storm days. Moreover, the result of Z_{xx} is stable, while that of Z_{xy} is unstable, and the phase of Z_{xy} rolls out of the normal quadrant. The storm result can be interpreted as the phenomenon of the PROQ case with a high SNR.

Moreover, we compare the MT sounding curves calculated by single-site and remote reference data processing

at site 130 in Fig. 12. Site 151 is used as the remote reference site. All the results coincide with each other. However, the non-storm-RR result is more scattered, and the error bar is larger than the storm result. Comparing the single-site and remote reference processing results shows that we can obtain a reliable result despite using single-site processing calculated by storm data.

Case study 2: USArray, USA

In the first case study, an intensive geomagnetic storm was chosen, and we chose a less intensive one in the second case study. The second field dataset was observed at site TNV48 from the USArray project (Schultz et al.

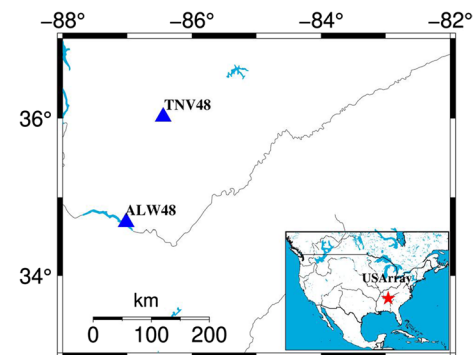


Fig. 13 Location map of the second field data. The blue triangles denote the observation site. TNV48 is used as the locale site, and ALW48 is set as the remote reference site. The right map shows the survey location of the USArray, and the red star denotes the location of site TNV48

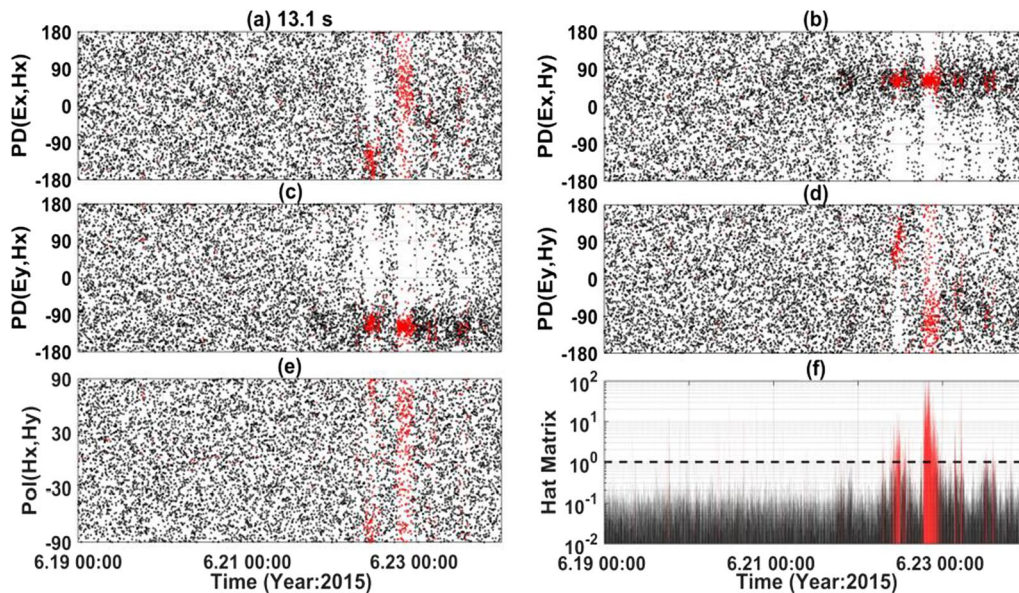


Fig. 14 Evaluation indices in the period of 13.1 s using the data observed from June 19 to June 24 at site TNV48. The data in red correspond to the leverage data associated with the storm. There are preferred directions of the PD corresponding to the leverage data, as shown in **b** and **c**

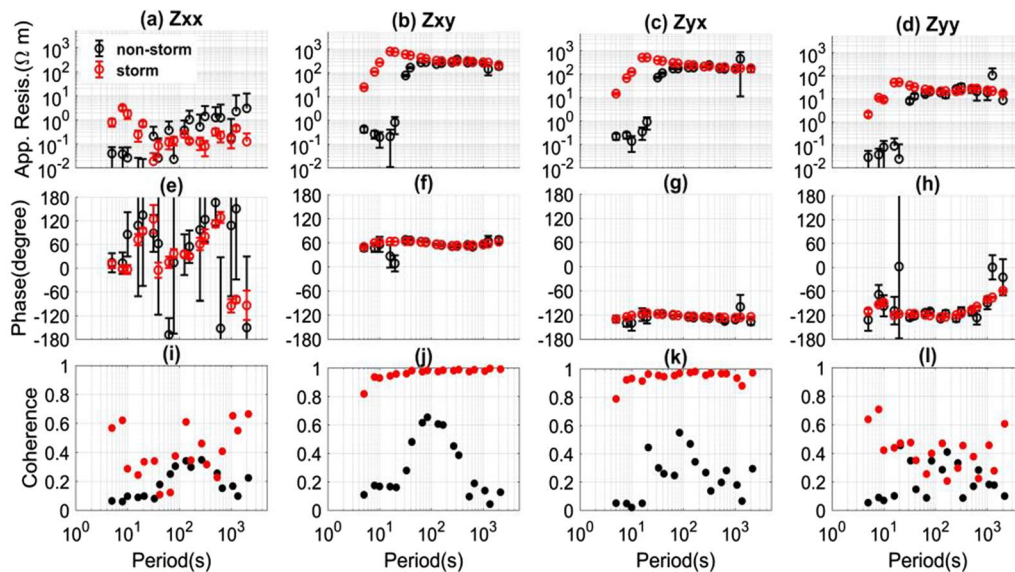


Fig. 15 MT sounding curves and coherence distributions during the storm and non-storm days using the data observed at TNV48 from USArray. The black color indicates the results calculated by non-storm data observed from 00:00 on June 19 to 00:00 on June 21; the red color indicates the results calculated by storm data observed from 00:00 on June 22 to 00:00 on June 24

2006–2018; Kelbert et al. 2018), as shown in Fig. 13. The time-series data can be downloaded from the Incorporated Research Institutions for Seismology (IRIS, see the website in references). The datasets were recorded for approximately 2 weeks in 2015, and the sampling period was 1 s. The geomagnetic storm started at approximately

18:00 on June 22 and ended at approximately 00:00 on June 24 (see Additional file 1: Figs. S5).

A similar analysis with KAP03 is performed on TNV48. At first, the data quality analysis in the period of 13.1 s is performed. The data observed from June 19 to June 24 are used. Figure 14b, c shows that $PD(E_x, H_y)$ and $PD(E_y, H_x)$ have a preferred direction corresponding to the leverage point.

Because the natural signal around the dead band (0.1–10 s) is relatively low, it can be easily influenced by local noise. When there is a geomagnetic storm, the natural EM signal's strength increases, the SNR becomes high, and a preferred direction of PD between the orthogonal electric and magnetic fields appears. The data in red can be categorized into a 1-D/2-D case with a high SNR. The black data are dominated by incoherent noise, and all the corresponding PD is scattered.

Next, we discuss the MT impedance quality during the storm and non-storm days at TNV48. Figure 15 shows MT sounding curves and coherence distributions during the storm and non-storm days. The non-storm data observed from June 19 to June 21 and storm data from June 22 to June 24 are used. The coherence value between the orthogonal electric and magnetic fields increased and was close to 1 during the storm. The low coherence during the non-storm day may be attributed to incoherent noise. The apparent resistivity of the non-storm result in the period from 8 to 30 s is severely down-biased, and the phase error bar is larger than that of the storm result. We think that incoherent noise leads to severely down-biased impedance between 8 and 30 s during the non-storm days.

Finally, we also compare the MT sounding curves calculated by single-site and remote reference data processing. The data observed at site ALW48 are used as the remote site. Figure 16 compares the MT sounding curves calculated by single-site and remote

reference data processing using storm and non-storm data. All the results coincide in a period longer than 40 s. However, the storm result is down-biased compared with the storm-RR result below 40 s; the storm data also contain intermittent incoherent noise. The remote reference can remove such kinds of noise. A more reliable result can be obtained using storm data with remote reference processing. On the other hand, the non-storm-RR result is scattered below 40 s because continuous incoherent noise dominates the non-storm data, according to the data quality analysis in Fig. 14.

Since the natural EM signal is relatively low in the dead band (0.1–10 s) and the local noise can easily influence it during the non-storm day, it is difficult to obtain a reliable impedance by robust and remote reference processing when the SNR is low all the time. When there is a geomagnetic storm, the natural EM signal's strength increases, high SNR data may appear, and we can obtain a more reliable impedance by using the storm data. We found similar situations at the USArray sites as follows: CON20, CON21, CON24, IAJ34, IAJ36, IAK35, IAK36, IAK39, IAK40, IAL36, IAL41, ILN42, KSP33, KSP36, KSR37, KSS35, KSS37, MIC40, MIE40, MND36, MND38, MNE35, MNG36, MTB22, MTD23, NDC31, NDE30, NDF27, NDF30, NVM11, REH36, SDI31, UTO13, UTO19, UTP13, UTP18, UTQ16, WIG39, WIG40, WYM17, WYM20, and WYM22.

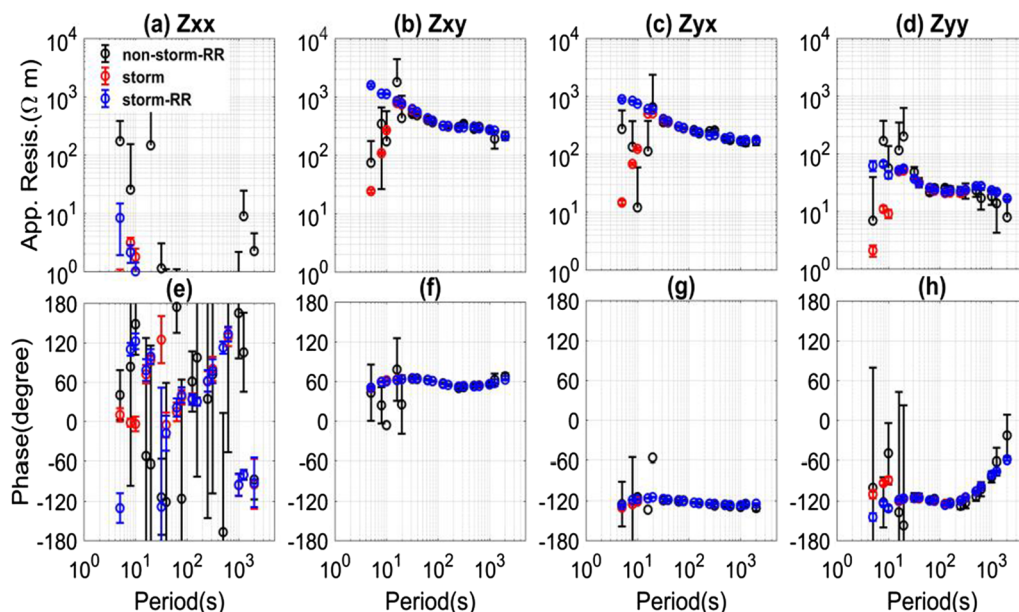


Fig. 16 Comparison of the MT sounding curves calculated by single-site and remote reference data processing using the storm and non-storm data observed at site TNV48. **a–d** Show the apparent resistivity. **e–h** Show the impedance phase. The horizontal axis denotes the period in seconds. The MT sounding curves longer than 40 s are similar and cover the XY and YX components

Discussion

First, we discuss how to analyze the data quality; the characteristics of the 1-D/2-D case present low coherence between the parallel electric and magnetic fields and high coherence between the orthogonal components. In contrast, the characteristics of PROQ present high coherence between the parallel electric and magnetic fields and low coherence between the orthogonal components. When the coherence is high, there is a preferred direction of PD. For 1-D/2-D or PROQ situations with good quality, there is always a preferred direction of PD between the corresponding electric and magnetic fields. On the other hand, the time-series data contaminated by coherent noise also have high coherence values and a preferred direction in PD. Therefore, we combine the polarization direction to confirm whether the coherent noise contaminates the data. There is no preferred polarization direction for the magnetic field in a quiet EM environment. If the magnetic field has a preferred polarization direction, we can consider that the data are contaminated by coherent noise in that period.

Moreover, the hat matrix is a parameter used to visualize the energy variation (see the example in Fig. 4). Therefore, we can combine the phase difference between the electric and magnetic fields, the polarization direction and the hat matrix to discuss how the data quality varies with energy changes for a specific period.

Next, we discuss the relationship between impedance and coherence. According to the least-squares theory (Sims et al. 1971), for the north–south direction, Z_{xy} can be calculated as follows:

$$Z_{xy} = \frac{\langle \mathbf{E}_x \tilde{\mathbf{H}}_y \rangle \langle \mathbf{H}_x \tilde{\mathbf{H}}_x \rangle - \langle \mathbf{E}_x \tilde{\mathbf{H}}_x \rangle \langle \mathbf{H}_x \tilde{\mathbf{H}}_y \rangle}{\langle \mathbf{H}_y \tilde{\mathbf{H}}_y \rangle \langle \mathbf{H}_x \tilde{\mathbf{H}}_x \rangle - \langle \mathbf{H}_y \tilde{\mathbf{H}}_x \rangle \langle \mathbf{H}_x \tilde{\mathbf{H}}_y \rangle} = \frac{C - D}{F - G}, \quad (13)$$

For the numerator of Eq. 13, there is a relationship with the coherence as follows:

$$|C| = \left| \langle \mathbf{E}_x \tilde{\mathbf{H}}_y \rangle \langle \mathbf{H}_x \tilde{\mathbf{H}}_x \rangle \right| = \text{coh}(\mathbf{E}_x, \mathbf{H}_y) \sqrt{\langle \mathbf{E}_x \tilde{\mathbf{E}}_x \rangle \langle \mathbf{H}_y \tilde{\mathbf{H}}_y \rangle \langle \mathbf{H}_x \tilde{\mathbf{H}}_x \rangle}, \quad (14)$$

$$|D| = \left| \langle \mathbf{E}_x \tilde{\mathbf{H}}_x \rangle \langle \mathbf{H}_x \tilde{\mathbf{H}}_y \rangle \right| = \text{coh}(\mathbf{E}_x, \mathbf{H}_x) \sqrt{\langle \mathbf{E}_x \tilde{\mathbf{E}}_x \rangle \langle \mathbf{H}_x \tilde{\mathbf{H}}_x \rangle \text{coh}(\mathbf{H}_x, \mathbf{H}_y) \sqrt{\langle \mathbf{H}_x \tilde{\mathbf{H}}_x \rangle \langle \mathbf{H}_y \tilde{\mathbf{H}}_y \rangle}}, \quad (15)$$

$$\frac{|C|}{|D|} = \frac{\left| \langle \mathbf{E}_x \tilde{\mathbf{H}}_y \rangle \langle \mathbf{H}_x \tilde{\mathbf{H}}_x \rangle \right|}{\left| \langle \mathbf{E}_x \tilde{\mathbf{H}}_x \rangle \langle \mathbf{H}_x \tilde{\mathbf{H}}_y \rangle \right|} = \frac{\text{coh}(\mathbf{E}_x, \mathbf{H}_y)}{\text{coh}(\mathbf{E}_x, \mathbf{H}_x) \text{coh}(\mathbf{H}_x, \mathbf{H}_y)}, \quad (16)$$

For the denominator of Eq. 13, there is a relationship with the coherence as follows:

$$|F| = \left| \langle \mathbf{H}_x \tilde{\mathbf{H}}_x \rangle \langle \mathbf{H}_y \tilde{\mathbf{H}}_y \rangle \right|, \quad (17)$$

$$|G| = \left| \langle \mathbf{H}_y \tilde{\mathbf{H}}_x \rangle \langle \mathbf{H}_x \tilde{\mathbf{H}}_y \rangle \right| = \text{coh}^2(\mathbf{H}_x, \mathbf{H}_y) \langle \mathbf{H}_x \tilde{\mathbf{H}}_x \rangle \langle \mathbf{H}_y \tilde{\mathbf{H}}_y \rangle, \quad (18)$$

$$\frac{|F|}{|G|} = \frac{1}{\text{coh}^2(\mathbf{H}_x, \mathbf{H}_y)}. \quad (19)$$

Because various sources generate natural magnetic signals, they generate magnetic fields that vary in their incident directions, which means that \mathbf{H}_x and \mathbf{H}_y are not coherent, and $\text{Coh}(\mathbf{H}_x, \mathbf{H}_y)$ is a small value. Under the condition that the coherence value between the orthogonal component $\text{Coh}(\mathbf{E}_x, \mathbf{H}_y)$ is relatively high, the coherence value between the parallel component $\text{Coh}(\mathbf{E}_x, \mathbf{H}_x)$ is small. The C part dominates the numerator of Eq. 13, and the F part dominates the denominator. Therefore, in the case where $\text{Coh}(\mathbf{E}_x, \mathbf{H}_y)$ is high and $\text{Coh}(\mathbf{E}_x, \mathbf{H}_x)$ is small, Z_{xy} can be rewritten as follows:

$$Z_{xy} \approx \frac{C}{F} = \frac{\langle \mathbf{E}_x \tilde{\mathbf{H}}_y \rangle}{\langle \mathbf{H}_y \tilde{\mathbf{H}}_y \rangle}. \quad (20)$$

In this situation, Z_{xy} is determined by the orthogonal electric and magnetic fields. The field data can be explained as the 1-D/2-D cases.

In contrast, if the coherence between the orthogonal component $\text{Coh}(\mathbf{E}_x, \mathbf{H}_y)$ is relatively low, while the coherence between the parallel component $\text{Coh}(\mathbf{E}_x, \mathbf{H}_x)$ is high. There is no Eq. 20. In that case, Z_{xy} is undetermined by the orthogonal electric and magnetic fields, and the phenomenon of PROQ may appear.

Finally, we discuss the different influences of strong and weaker storms on the impedance calculation. There are three cross-power spectra densities ($\langle \mathbf{E}_x \tilde{\mathbf{H}}_x \rangle$, $\langle \mathbf{E}_x \tilde{\mathbf{H}}_y \rangle$, $\langle \mathbf{H}_x \tilde{\mathbf{H}}_y \rangle$) and two autopower spectra densities ($\langle \mathbf{H}_x \tilde{\mathbf{H}}_x \rangle$, $\langle \mathbf{H}_y \tilde{\mathbf{H}}_y \rangle$) in Eq. 13. The energy of the signal and noise vary with time; therefore, the SNR varies with time, and we can rewrite the cross-

power and autopower spectra densities as follows:

$$\langle \mathbf{A} \tilde{\mathbf{B}} \rangle = \langle \mathbf{A}^S \tilde{\mathbf{B}}^S \rangle + \langle \mathbf{A}^N \tilde{\mathbf{B}}^N \rangle, \quad (21)$$

$$\langle \mathbf{A} \tilde{\mathbf{A}} \rangle = \langle \mathbf{A}^S \tilde{\mathbf{A}}^S \rangle + \langle \mathbf{A}^N \tilde{\mathbf{A}}^N \rangle, \quad (22)$$

where $\langle A^S \overline{A^S} \rangle$ and $\langle A^S \overline{B^S} \rangle$ are the autopower and cross-power spectra densities calculated by the high SNR data and $\langle A^N \overline{B^N} \rangle$ and $\langle A^N \overline{A^N} \rangle$ are the autopower and cross-power spectra densities calculated by the low SNR data. The noise influences the cross-power and autopower spectra density between the electric and magnetic fields, influencing the impedance calculation of Eq. 13.

In the situation of a very strong storm, such as the first case study, the energy also varies intensely during the storm. On the one hand, the amplitude of the leverage point can sometimes be 100 times that with low-energy data, as shown in Fig. 4. The influence of the high SNR data on the spectra is 10,000 times that of the low SNR data. On the other hand, the storm lasts a long time in a very strong storm, which means that the proportion of data with high SNR is high. At that time, $\langle A^N \overline{B^N} \rangle$ and $\langle A^N \overline{A^N} \rangle$ can be neglected compared with $\langle A^S \overline{A^S} \rangle$ and $\langle A^S \overline{B^S} \rangle$. Examples of sites 130 and 142 of KAP03 show that the single-site result coincides with the remote reference result calculated by storm data. Although using single-site processing, we can obtain a reliable result in a very strong storm.

In the case of a less intense storm, such as the second case study, the intensity is smaller than that in the first case study and lasts a shorter time, which means that the proportion of high SNR data is low. In this situation, $\langle A^N \overline{B^N} \rangle$ and $\langle A^N \overline{A^N} \rangle$ cannot be neglected compared with $\langle A^S \overline{A^S} \rangle$ and $\langle A^S \overline{B^S} \rangle$. Even if high SNR data are observed, it is not sufficient to obtain a reliable result using single-site processing; in this case, remote reference technology (Gamble et al. 1979) may reduce the influence of noise. We can see the example at site TNV48 of USArray. Assuming that the remote site is unavailable, we can also use the preselection strategy, e.g., the method proposed by Weckmann et al. (2005), to extract the high SNR data and obtain a reliable impedance.

Conclusions

In a quiet EM environment, the proportion of high SNR data is high enough to obtain a reliable impedance during the storm and non-storm days; therefore, the impedance results calculated by storm and non-storm data are similar. This situation was shown by the data observed at site 163 of KAP03. The storm does not influence the impedance result.

In a noisy EM environment, artificial noise dominates the data quality during non-storm days, especially for the data around the dead band (0.1 to 10 s) since the natural EM signal is relatively low. When there is a geomagnetic storm, the natural EM signal's strength increases, high SNR data may appear, and we can obtain a more reliable impedance using the storm data. This situation was shown by the data observed at site TNV48 of USArray and sites 130 and 142 of KAP03.

Artificial disturbances to EM measurements are becoming more and more serious, especially in urban areas. The measurements occasionally contain the artificial noise all the time, which is difficult to remove using the current techniques. High SNR data may appear when there is a storm, and it is possible to obtain a reliable result by the preselection strategy or remote reference processing. It might be useful to perform the MT campaign during geomagnetic storms if we need to resurvey at the noisy sites. Utilizing the data observed during a geomagnetic storm may overcome the local noise's influence and obtain a more reliable and interpretable impedance, although the site is contaminated by the noise all the time.

Supplementary Information

The online version contains supplementary material available at <https://doi.org/10.1186/s40623-022-01659-6>.

Additional file 1. Statistical analysis of geomagnetic storm using the Dst index and the variation in the Dst index for the second case study.

Acknowledgements

This work was supported by JST SPRING, Grant Number JPMJSP2136. We thank all SAMTEX and USArray team members for providing the time-series data used in this study. We thank INTERMAGNET (International Real-time Magnetic Observatory Network) for providing the magnetic time-series data observed at the KAK station. We thank the WDC for Geomagnetism, Kyoto, for providing the Dst index data to analyze the geomagnetic storm. Finally, we express special thanks to Maik Neukirch, Benjamin Murphy and Peng Han for their constructive comments to improve the manuscript. We also thank Ute Weckmann, Louise Alexander, Takeshi Sagiya and several anonymous reviewers who reviewed the manuscript and gave us constructive comments to improve the manuscript.

Author contributions

Hao Chen processed the time-series data, generated the results and wrote the paper. Hao Chen contributed approximately 60%. Hideki Mizunaga reviewed the paper and contributed approximately 30%; Toshiaki Tanaka contributed approximately 10% to this work. All authors read and approved the final manuscript.

Funding

This work was supported by JST SPRING, Grant Number JPMJSP2136.

Availability of data and materials

The SAMTEX team provided the time-series data of KAP03, which can be downloaded from MTNET (see the website in the reference). The USArray team provided the time-series data of TNV48, which can be downloaded from IRIS (see the website in the reference). The Dst index data can be downloaded from the WDC for Geomagnetism, Kyoto (<http://wdc.kugi.kyoto-u.ac.jp/dstdir/index-j.html>). The magnetic time-series data observed at the KAK station can be downloaded from INTERMAGNET (International Real-time Magnetic Observatory Network). Alan Chave provided the BIRRP code.

Competing interests

We know of no conflicts of interest associated with this publication. We declare that this manuscript is original, has not been previously published and is not currently being considered for publication elsewhere.

Author details

¹Department of Earth Resources Engineering, Graduate School of Engineering, Kyushu University, Fukuoka 819-0395, Japan. ²Department of Earth Resources Engineering, Faculty of Engineering, Kyushu University, Fukuoka 819-0395, Japan.

Received: 27 August 2021 Accepted: 8 June 2022

Published online: 20 July 2022

References

- Cagniard L (1953) The basic theory of the magneto-telluric method of geophysical prospecting. *Geophysics* 18:605–635
- Chave AD, Jones AG (2012) The magnetotelluric method: theory and practice. Cambridge University Press, Cambridge
- Chave AD, Thomson DJ (2003) A bounded influence regression estimator based on the statistics of the hat matrix. *J R Stat Soc Ser C* 52:307–322
- Chave AD, Thomson DJ (2004) Bounded influence estimation of magnetotelluric response functions. *Geophys J Int* 157:988–1006
- Chave AD, Thomson DJ, Ander ME (1987) On the robust estimation of power spectra, coherences, and transfer functions. *J Geophys Res Solid Earth* 92:633–648
- Chouteau M, Tournier B (2000) Analysis of magnetotelluric data showing phase rolling out of quadrant (PROQ). SEG Technical Program Expanded Abstracts 2000, Society of Exploration Geophysicists, pp. 344–346.
- Constable C (2016) Earth's electromagnetic environment. *Surv. Geophysics* 37:27–45
- Constable CG, Constable SC (2004) Satellite magnetic field measurements: applications in studying the deep Earth. *State Planet Front Chall. Geophysics* 19:147
- Egbert GD (1997) Robust multiple-station magnetotelluric data processing. *Geophys J Int* 130:475–496
- Egbert GD, Booker JR (1986) Robust estimation of geomagnetic transfer functions. *Geophys J R Astr Soc* 87:173–194
- Egbert GD, Livelybrooks DW (1996) Single station magnetotelluric impedance estimation: Coherence weighting and the regression M-estimate. *Geophysics* 61:964–970
- Egbert GD, Eisel M, Boyd OS, Morrison HF (2000) DC trains and Pc3s: Source effects in mid-latitude geomagnetic transfer functions. *Geophys Res Lett* 27:25–28
- Fontes SL, Harinarayana T, Dawes GJK, Hutton VRS (1988) Processing of noisy magnetotelluric data using digital filters and additional data selection criteria. *Phys Earth Planet Inter* 52:30–40
- Fowler RA, Kotick BJ, Elliott RD (1967) Polarization analysis of natural and artificially induced geomagnetic micropulsations. *J Geophys Res* 72:2871–2883
- Gamble TD, Goubau WM, Clarke J (1979) Magnetotellurics with a remote reference. *Geophysics* 44:53–68
- Garcia X, Jones AG (2002) Atmospheric sources for audio-magnetotelluric (AMT) sounding. *Geophysics* 67:448–458
- Garcia X, Chave AD, Jones AG (1997) Robust processing of magnetotelluric data from the auroral zone. *J Geomagn Geoelectr* 49:1451–1468
- Hennessy L, Macnae J (2018) Source-dependent bias of sferics in magnetotelluric responses. *Geophysics* 83:E161–E171
- IRIS, http://ds.iris.edu/gmap/#network=_US-MT&planet=earth
- Jones AG, Evans RL, Muller MR, Hamilton MP, Miensopust MP, Garcia X, Cole P, Ngwisanyi T, Hutchins D, Fourie CJS (2009) Area selection for diamonds using magnetotellurics: examples from southern Africa. *Lithos* 112:83–92
- Jones, A.G., Jödicke, H., 1984. Magnetotelluric transfer function estimation improvement by a coherence-based rejection technique. In: SEG Technical Program Expanded Abstracts 1984, Society of Exploration Geophysicists, pp. 51–55.
- Junge A (1996) Characterization of and correction for cultural noise. *Surv Geophys* 17:361–391
- Kelbert A, Erofeeva S, Trabant C, Karstens R, Van Fossen M (2018) Taking magnetotelluric data out of the drawer. *Eos*. <https://doi.org/10.1029/2018E0112859>
- Lezaeta P, Chave A, Jones AG, Evans R (2007) Source field effects in the auroral zone: evidence from the Slave craton (NW Canada). *Phys Earth Planet Inter* 164:21–35
- Mareschal M (1981) Source effects and the interpretation of geomagnetic sounding data at sub-auroral latitudes. *Geophys J Int* 67:125–136
- Mareschal M (1986) Modelling of natural sources of magnetospheric origin in the interpretation of regional induction studies: a review. *Surv Geophys* 8:261–300
- Marple SL, Marino C (2004) Coherence in signal processing: a fundamental redefinition. Conference Record of the Thirty-Eighth Asilomar Conference on Signals, Systems and Computers, 2004, IEEE, pp. 1035–1038.
- McPherron RL (2005) Magnetic pulsations: their sources and relation to solar wind and geomagnetic activity. *Surv Geophysics* 26:545–592
- MTNET, <https://www.MTnet.info/data/kap03/kap03.html>.
- Murphy BS, Egbert GD (2018) Source biases in midlatitude magnetotelluric transfer functions due to Pc3–4 geomagnetic pulsations. *Earth Planets Space* 70:1–9
- Oettinger G, Haak V, Larsen JC (2001) Noise reduction in magnetotelluric time-series with a new signal–noise separation method and its application to a field experiment in the Saxonian Granulite Massif. *Geophys J Int* 146:659–669
- Rikitake T (1948) 1. Notes on electromagnetic induction within the Earth. *Bull. Earthquake Res Inst* 24:1–9
- Schultz A, Egbert GD, Kelbert A, Peery T, Clote V, Fry SB (2006–2018) Erofeeva and staff of the National Geoelectromagnetic Facility and their contractors (2006–2018), USArray TA MT Transf Funct. <https://doi.org/10.17611/DP/EMTF/USARRAY.TA>.
- Sims WE, Bostick FX, Smith HW (1971) The estimation of magnetotelluric impedance tensor elements from measured data. *Geophysics* 36:938–942
- Singh A, Rathore VS, Singh RP, Singh AK (2017) Source identification of moderate ($-100 \text{ nT} < \text{Dst} < -50 \text{ nT}$) and intense geomagnetic storms ($\text{Dst} < -100 \text{ nT}$) during ascending phase of solar cycle 24. *Adv Space Res* 59:1209–1222
- Smirnov MY (2003) Magnetotelluric data processing with a robust statistical procedure having a high breakdown point. *Geophys J Int* 152:1–7
- Sugiura M, Kamei T (1991) Masahisa Sugiura Note added in June 1991. <https://wdc.kugi.kyoto-u.ac.jp/dstdir/dst2/onDstindex.html>
- Szarka L (1988) Geophysical aspects of man-made electromagnetic noise in the Earth-A review. *Surv Geophys* 9(3–4):287–318
- Tikhonov AN (1950) On determining electrical characteristics of the deep layers of the Earth's crust in Doklady. Citeseer, State College, pp 295–297
- Tsurutani BT, Gonzalez WD, Gonzalez AL, Guarnieri FL, Gopalswamy N, Grande M, Kamide Y, Kasahara Y, Lu G, Mann I (2006) Corotating solar wind streams and recurrent geomagnetic activity: a review. *J Geophys Res Space Phys*. <https://doi.org/10.1029/2005JA011273>
- Viljanen A, Pirjola R, Häkkinen L (1993) An attempt to reduce induction source effects at high latitudes. *J Geomagn Geoelectr* 45(9):817–831
- Weckmann U, Ritter O, Haak V (2003) A magnetotelluric study of the Damara Belt in Namibia: 2. MT phases over 90 reveal the internal structure of the Waterberg Fault/Omaruru Lineament. *Phys Earth Planet Inter* 138:91–112
- Weckmann U, Magunia A, Ritter O (2005) Effective noise separation for magnetotelluric single site data processing using a frequency domain selection scheme. *Geophys J Int* 161:635–652
- Yu G, Xiao Q, Li M (2018) Anisotropic model study for the phase roll out of quadrant data in magnetotellurics. *Chin J Geophys* 62(2):763–778
- Zonge KL, Hughes LJ (1987) Controlled source audio-frequency magnetotellurics. In: Nabighian MN (ed) *Electromagnetic methods in applied geophysics applications*. SEG, Houston, pp 713–809

Publisher's Note

Springer Nature remains neutral with regard to jurisdictional claims in published maps and institutional affiliations.

Submit your manuscript to a SpringerOpen[®] journal and benefit from:

- Convenient online submission
- Rigorous peer review
- Open access: articles freely available online
- High visibility within the field
- Retaining the copyright to your article

Submit your next manuscript at ► [springeropen.com](https://www.springeropen.com)